Real-Time Imaging 8, 475–490 (2002)
doi:10.1006/rtim.2001.0290, available online at http://www.idealibrary.com on IDEAL®

# Biological Image Restoration in Optical-Sectioning Microscopy Using Prototype Image Constraints

The deconvolution of images obtained by means of optical-sectioning widefield fluorescence microscopy, is a relevant problem in biological applications. Several methods have been proposed in the last few years, with different degrees of success, to improve the quality of the images, but the data complexity and the computational cost remain a limiting factor in this problem. We present in this paper an approach to perform the deconvolution of three-dimensional data obtained by fluorescence microscopy (widefield) based on the Projection onto Convex Sets theory. Initially, a brief review of the Projection onto Convex Sets theory is presented. In the restoration algorithm, we combine some constraint sets to restore the out-of-focus blur, to reduce the Poisson noise due to the acquisition process, to retrieve the missing frequencies due to the transfer function of the optical system, and to prevent the regularization errors. Some examples using a phantom and real cell images are presented. The method demonstrates good performance in terms of both visual results and cost–benefit analysis.



**M.R.P. Homem[1], N.D.A. Mascarenhas[2], L.F. Costa[1] and C. Preza[3]**

*[1]Cybernetic Vision Research Group, Instituto de Física de São Carlos*
*Universidade de São Paulo, USP – Av. Trabalhador São Carlense, 400*
*CEP:13.566-590, São Carlos, SP, Brazil*
*E-mail: {murillo, luciano}@if.sc.usp.br*
*[2]Departamento de Computação, Universidade Federal de São Carlos*
*UFSCar – Via Washington Luís, Km 235, CP 676,*
*CEP: 13.565-905, São Carlos, SP, Brazil*
*E-mail: nelson@dc.ufscar.br*
*[3]Electrical Engineering Department, Washington University, St. Louis, MO 63130, USA*
*E-mail: preza@ee.wustl.edu*

## Introduction

Three-dimensional (3D) real-time processing in computational optical-sectioning microscopy (COSM) still remains an open problem in biological applications because of the data complexity and the computational cost of processing. Nevertheless, the visualization of the proper 3D image of a biological specimen is substantially important in many specific problems, because the cell structure (or its components) and its function are strongly correlated. Especially, in neuroscience, the visualization and description of each cellular structure play an important role in neuromorphometric studies, where, for instance, it is known that functional properties of a neuron are connected with physical boundaries of its membrane [1]. In this sense, the proper visualiza-

1077-2014/02/$35.00 

tion of the 3D neuron image is necessary for a complete understanding of the nervous cells. Therefore, the processing and visualization of 3D neuron images can be a powerful tool in neuroscience.

Computational optical sectioning using confocal or conventional widefield fluorescence microscopy is able to provide 3D data sets of living cells [2]. However, due to limiting factors in the imaging systems, microscopic images are degraded by the microscope optics and by the detection process. Each slice of the 3D image is blurred, i.e. it has contributions of light from other out-of-focus planes. Also, the Fourier transform (FT) of the point spread function (PSF) of the microscope, i.e. the transfer function (TF), is zero valued for most of the frequencies in the Fourier domain. This is due to the circular aperture of the microscope and in the region where it has non-zero values it works as a low-pass filter and in the regions where it has zero values it removes the image content in that region. Then, it is important to search for algorithms that are able to deblur the images and also to recover the missing Fourier components into the missing cone region [3] and for the other non-zero regions.

The decision to use confocal or widefield microscopy depends on the application. The former modality is able to produce high-quality images because only the light from the region near the in-focus plane is detected, but the cost of such equipment is still substantially high. In confocal microscopy, the light efficiency and sensitivity are less than in a conventional microscope, which can be a problem in experiments where the light efficiency is important such as imaging of living specimens. On the other hand, widefield microscopes are cheaper than confocal ones. Widefield microscopy is particularly valuable for work with living specimens, because it avoids specimen damage due to the laser light used in confocal microscopy, and also because it allows imaging with wavelengths not provided by standard lasers.

Despite the powerful computers currently available, the large size of the data set and the computational cost of processing these data are often limiting factors in many practical applications that involve time-lapse studies of living specimens. The search for more effective and faster algorithms came over to produce better-quality microscopic images with less computational cost, allowing to improve experiments where the time demand is critical as, for instance, in the study of living cells. The problem that arises is to devise efficient algorithms that are able to improve the image quality in widefield fluorescence microscopy in a short processing time. It is noted that such algorithms can be applied to confocal images to further improve the resolution of the images [4].

Besides the blurring due to the microscope optics, there are several sources of noise that decrease the quality of the images. As a result of the many problems that arise when imaging living cells (for instance, to avoid photobleaching), the images are often recorded under low-level light. In these situations, the images are quantum limited and they are corrupted by the Poisson noise. Also, other noise sources come from the CCD camera systems that are usually used to record the images.

The problem of recovering the specimen function (in this case, the fluorescence concentration) from the observed blurred and noisy image is often referred to as "deconvolution". Over the last 20 years, several different algorithms with different complexity and processing time have been developed to solve this problem [5, 6, 7, 8]. Linear, non-iterative, true 3D "deconvolution" methods such as the regularized linear least squares (*RLLS*) algorithm proposed by Preza *et al.* [9, 10] are the fastest, however, they cannot recover the missing Fourier components. In principle, non-linearity is necessary in order to recover the missing frequencies as was shown in [11]. However, if one desires a first estimate, the *RLLS* is able to give a good first approximation of the true image. Better approximations can be obtained with iterative and non-linear algorithms (for a comparison of several such methods see [8] and [12]). One widely used method is the maximum likelihood expectation maximization algorithm (*MLEM*) [13] applied to microscopy by several investigators [14, 15]. Algorithms based on the *MLEM* method provide a better combination of robustness to noise and super-resolution capabilities (i.e. they can recover some of the missing frequencies) than algorithms based on different approaches [4,16]. Unfortunately, the *MLEM* algorithm is impractical in applications where the processing speed is critical, because of its slow convergence.

In this paper, we present an alternative algorithm to perform the deconvolution of 3D data obtained by fluorescence microscopy, based on the projection onto convex sets (POCS) methodology where the idea is to show how the projection methods can be a good tool to perform deconvolution of 3D microscopic images.

The POCS approach has been applied in several areas as image and signal processing, neural networks, optics, etc. We refer the reader to [7–23] for good reviews on the subject.

Some attempts to use POCS for the restoration of 3D microscopic images were done, for instance, by Koshy *et al.* [24] where they have presented a POCS algorithm based on the Tikonov–Miller regularization. Lenz [25] proposed another algorithm that uses only a few slices close to the focal plane to perform the restoration. Gopalakrishman *et al.* [26] proposed an alternative algorithm using the row action procedure in such a problem. All these approaches do not take into account the presence of Poisson noise. Koshy does not present concluding studies. The algorithm using the row action procedure shows a slow convergence rate and the Lenz algorithm does not have experimental results.

The work proposed in this paper uses an approach based on prototype-images constraints, which have been proposed and analyzed by Sezan and Trussel [27]. We refer the reader to [27] and [28] for an overview of these constraints.

Following [27], we propose the use of sets based on the variation around the Wiener solution together with a pointwise adaptive smoothness constraint. Due to the presence of Poisson noise in the images, we suggest a pre-processing of the observed images in order to reduce this noise before the projections onto the constraint sets or, on the other hand, the use of the filter proposed by Goodman and Belsher [29] that takes into account the nature of the Poisson noise as a substitute for the Wiener solution. We also use constraints to ensure the positiveness of the solution, to prevent regularization errors, and to achieve super-resolution by reinforcing the finite extent constraint of the estimated image.

This paper is organized as follows: First, in the following section, the image formation model together with a characterization of the noise is presented. In the next section, a brief review of the serial cyclic POCS theory and the constraints sets are presented. The section on the Poisson Noise Filtering Procedures explains the procedures for reducing the Poisson noise and the section which follows it presents the POCS algorithm. Eventually, numerical results and discussions are presented in the subsequent sections.

## Problem Characterization

*Image-formation model*

In COSM, a 3D image is formed by stacking a series of 2D images (optical slices) that are acquired by using light microscopy. However, this technique of optical slicing has the disadvantage that each slice is obstructed by out-of-focus information, which affects each image from adjacent slices. The mechanism of degradation can be described by modeling the microscope's optics and the detection process [30]. In this paper, we are concerned with images obtained using the fluorescence technique. Consider an object function (specimen) as $f(x, y, z)$, where $(x, y, z) \in S$ are the 3D coordinates in the real space, where $S$ is the extent of $f(x, y, z)$, with a thickness $t$ modeled as a stack of $J$ 2D slices along the $z$-axis, such that $t = J \cdot \Delta z$.

By considering the blurring as a linear, space-invariant operator [3] and in the absence of noise, the $k$th observed slice is given by

$$b_k(x, y) = \sum_{j=0}^{J-1} \left[h_{k-j}(x, y) * f_j(x, y)\right] \tag{1}$$

for $h_{k-j}(x, y) = h(x, y, z_d)$, where $z_d = z_k - j \cdot \Delta z$, $h(x, y, z)$ is the 3D incoherent PSF, $f_j(x, y)$ is the $j$th section of the specimen and * denotes a 2D convolution. The function $h_{k-j}(x, y)$ can be viewed as the image of a point source in the $j$th section of the object when the microscope is focused on the $k$th slice at $z_k$.

The set of $K$ data images of Eqn (1) obtained by moving the focal plane along the optical axis is the result of the 3D discrete convolution of $f(x, y, z)$ with $h(x, y, z)$ over all the spatial dimensions. Then, we have that

$$b(x, y, z) = h(x, y, z) * f(x, y, z) \tag{2}$$

where $b(x, y, z)$ is the observed image, and now * denotes a 3D convolution.

We can write Eqn (2) in the Fourier domain as

$$B(u, v, w) = H(u, v, w) \cdot F(u, v, w) \tag{3}$$

where $B(u, v, w)$ is the FT of $b(x, y, z)$, $F(u, v, w)$ the FT of $f(x, y, z)$ and $H(u, v, w)$ is the FT of $h(x, y, z)$ and $(u, v, w)$ are the 3D coordinates in the Fourier space.

Without loss of generality, we can consider only 3D cubic images of size $N^3$ and using a lexicographic ordering vector notation we have

$$\mathbf{b} = \mathbf{H} \cdot \mathbf{f} \tag{4}$$

where $\mathbf{b}$ and $\mathbf{f}$ are $N^3 \times 1$ vectors that are formed by stacking the elements of $b(x,y,z)$ and $f(x, y, z)$, respectively. $\mathbf{H}$ is the $N^3 \times N^3$ blurring matrix that gives the blurring degradation effects, where the elements are samples of the 3D PSF $h(x, y, z)$.

*Noise characterization*

In this paper, we are concerned with only two sources of noise that can arise from COSM using fluorescence: a signal-dependent noise that can be modeled by a Poisson distribution and an additive, signal-independent noise.

Generally, the repeated exposures needed to generate the 3D data will bleach the fluorophores into the specimen. The more the time to get the image, the more significant the differences between the intensities of images at the beginning and the end of the stack of 2D images. This effect is known as photobleaching [2] and it is stronger when the specimen is a living cell, which does not respond well to bleach retardants. Although one can bleach correct the stacks after the acquisition, the effect of photobleaching can be minimized (not eliminated) with a short exposure time. However, the shorter the time of exposure, the lower the level of photon count we have. Under this condition, the images are subject to a kind of noise that is dependent on the signal and that can be modeled by a Poisson distribution. Other sources of noise can arise from the device used to record the images. A CCD camera is usually the normal way to record the images acquired in COSM. In this work, we are only interested in the CCD noise and no other imperfection of the camera is taken into account. Snyder [31] has shown that a random process that is additive and independent of the signal can model this type of noise. In this sense, we can consider that the observed image is corrupted by a signal-dependent Poisson noise due to the acquisition process and by a signal-independent, additive noise due to the recording system.

The additive and independent noise can be incorporated into the model of Eqn (2) by an additive term $\eta(x,y,z)$:

$$b(x,y,z) = h(x,y,z) * f(x,y,z) + \eta(x,y,z) \tag{5}$$

and in the Fourier domain

$$B(u,v,w) = H(u,v,w)F(u,v,w) + N(u,v,w) \tag{6}$$

where $N(u,v,w)$ is the FT of $\eta(x,y,z)$. In vector–matrix notation we have

$$\mathbf{b} = \mathbf{H}\cdot\mathbf{f} + \boldsymbol{\eta} \tag{7}$$

On the other hand, the Poisson noise is incorporated into Eqn (4) by considering the observation as an inhomogeneous Poisson process. Let **g** be the version of **b** degraded by Poisson noise. From the semi-classical theory of photon detection, the probability that $g_i$ photon events occur for a given fixed intensity $b_i$ is

$$p(g_i \backslash b_i) = \frac{(\lambda\cdot b_i)^{g_i} e^{-\lambda\cdot b_i}}{g_i!} \tag{8}$$

where $\lambda$ is a constant rate parameter, $g_i$ is an element of the image vector **g** and $b_i$ is an element of the image vector **b**. The mean and variance of $g_i$ for a given $b_i$ is $E[g_i] = \lambda\cdot b_i$ and $Var[g_i] = \lambda\cdot b_i$.

We are interested in determining the object intensity using the observed image and any other *a priori* information. Due to the fact that the inverse matrix of **H** in Eqn (7) may not exist and also due to the noise nature, this problem is an ill-posed inverse problem, in the sense that the slightest noise or error in the observed image can yield large variations in the estimated image.

## The Projections Methods

*POCS methodology*

POCS is an important result from vector–space projections theory. In this section, we present a brief review of the POCS theory. Given a set $C$ and any points $x_1, x_2 \in C$, then $C$ is convex if $x = \mu x_1 + (1-\mu)x_2 \in C$ for $0 \le \mu \le 1$.

Let $C_1, C_2, \ldots, C_M$ be $M$ closed and convex sets in a Hilbert space $H$ and $\text{Ø} \neq C = \cap_{m=1}^{M} C_m$. For each set $C_k$, $k \in I = \{1,\ldots,M\}$, where $I$ is an index family, there is a projector operator (or projector) $\mathbf{P}_k$ such that for each point (or function) $f \in H$ we have $\|f - \mathbf{P}_k\cdot f\| \le \|f - x\|$ over all $x \in C_k$. Then, the element nearest to $f$ in $C_k$ is $\mathbf{P}_k\cdot f$. It can be shown that if $C_k$ is closed and convex then $\mathbf{P}_k\cdot f$ is unique. For an arbitrary starting point $f^{(0)}$, a sequence $\{f^{(n)}\}$ is generated by the recursive relation

$$f^{(n+1)} = \mathbf{P}_M\cdot\mathbf{P}_{M-1}\cdot\ldots\cdot\mathbf{P}_1\cdot f^{(n)} \tag{9}$$

It can be shown that iterates $\{f^{(n)}\}$ will converge weakly to a point of $C$ [18]. Figure 1 shows a diagram of the method using only two sets. The recursive relation into Eqn (9) is the well-known cyclic POCS algorithm and in its relaxed version Eqn (9) has the form

$$f^{(n+1)} = \mathbf{T}_M\cdot\mathbf{T}_{M-1}\cdot\ldots\cdot\mathbf{T}_1\cdot f^{(n)} \tag{10}$$

where $\mathbf{T}_k$ is defined by $\mathbf{T}_k = \mathbf{I} - \lambda_{n,k}\cdot(\mathbf{P}_k - \mathbf{I})$ for $\lambda_{n,k} \in (0,2)$. In the general case, the relaxation parameter

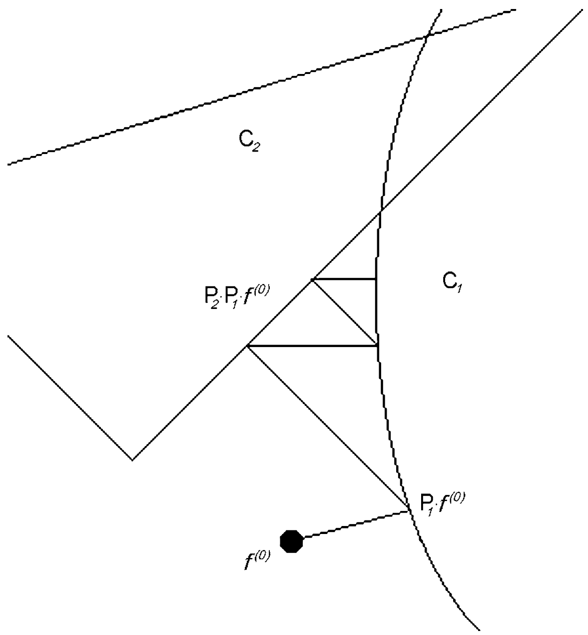


**Figure 1.** POCS algorithm using two sets. The sequence converges to $C_1 \cap C_2$.

depends on the projector and on the interaction step [18, 20].

*Image restoration using POCS*

In the image restoration problem, the algorithm searches for a solution (image) that is consistent with a number of *a priori* constraints, which are defined as convex sets. In this sense, the algorithm searches for an image in $C = \cap_{m=1}^{M} C_m$, where $C_k \in H$, $k \in I$ and each member of $C$ is a feasible solution of the problem. The regularization process can be viewed as enforcing the restoration result to satisfy all the constraint sets (*a priori* information). The image space is the finite 2D or 3D Euclidean space and iterates in Eqn (9) converge strongly to a feasible point in $C$.

In this paper, we use five closed convex sets to perform the restoration of 3D microscopic images. Two of them are intended to deconvolve the observed image with the PSF of the microscopic imaging system. They are based on the prototype constraints defined by Sezan [27] and use a bounded variation of the Wiener solution. It is well known that the Wiener filter is optimal under the framework of a linear estimator under additive, signal-independent noise, so in order to use this set we propose a pre-processing to reduce or minimize the signal-dependent Poisson noise and after that we assume that the remaining noise is approximately additive and independent of the signal. On the other hand, as an alternative to the suggested pre-processing step, which increases the global processing time, we propose the use of the Wiener filter under the Poisson criterion as suggested by Goodman and Belsher [29]. We also use a constraint set to ensure the positiveness of the solution, a constraint set based on the hypothesis of compact support (in order to recover the missing frequencies) and one to minimize the errors that arise from the regularization process into both the Wiener filter and the Goodman and Belsher filter.

*The prototype image constraints sets*

The discussion that follows is based on the work of Sezan and Trussell. For a detailed discussion, we refer the reader to [27]. In the general case, one can define these sets if it is possible to determine a prototype image and a bounded variation from that prototype. Using the lexicographic ordering, one can write in matrix–vector notation

$$C = \{\mathbf{y} : \|\mathbf{q} - \mathbf{y}\|^2 \leq \xi\} \tag{11}$$

where $\mathbf{q} \in \Re^L$ represents the prototype image, $\mathbf{y} \in \Re^L$ represents an arbitrary member of the set $C$ and the quantity $\xi$ represents the bounded variation between $\mathbf{y}$ and the prototype image vector $\mathbf{q}$. This kind of constraints can also be defined in the frequency domain as

$$C = \{\mathbf{y} : \|\mathbf{Q} - \mathbf{Y}\|^2 \leq \xi\} \tag{12}$$

where $\mathbf{Q}$ and $\mathbf{Y}$ are the discrete Fourier transform (DFT) of $\mathbf{q}$ and $\mathbf{y}$, respectively.

We can define as many sets as the number of elements of $\mathbf{q}$, i.e.

$$C_l = \{\mathbf{y} : \|q(l) - y(l)^2\| \leq \xi(l)\} \tag{13}$$

where $l = 1, \ldots, L$, $L = N^3$. Then, we have a family of sets where each one corresponds to one specific spatial position.

If we construct the projectors $\mathbf{P}_{C_l}$, $l = 1, \ldots, L$ for all the sets in Eqn (13), the projector $\mathbf{P}_C$ for the set $C$ in Eqn (11) is defined by the composition

$$\mathbf{P}_C = \mathbf{P}_{C_1} \circ \mathbf{P}_{C_2} \ldots \mathbf{P}_{C_L} \tag{14}$$

In practice, prototype images are usually obtained from the observed image as a result of applying a predetermined linear operator $\mathbf{q} = \mathbf{O} \cdot \mathbf{g}$ and $\boldsymbol{\xi}$ is obtained by $\boldsymbol{\xi} = c \cdot \boldsymbol{\psi}$, where $c$ is a positive constant and $\boldsymbol{\psi} = E\{\|\mathbf{q} - \mathbf{f}\|^2\}$ which is the expected variation when the true solution is known. The user chooses the constant $c$ and it is determined by the confidence that we have about the constraint set.

*Prototype constraint based on the Wiener solution*

Based on the preceding section, we will define three of the sets used in this paper. Sezan and Trussell [27] defined a set based on the adaptation of the Wiener solution for the 2D case. Here, we present the extension for the 3D case. For a particular triple of frequencies $(u, v, w)$, assume that the operator $\mathbf{O}$ is the pointwise parametric Wiener filter defined in the Fourier domain for the 3D case by

$$W(u, v, w) = \frac{\bar{H}(u, v, w)\Phi_f(u, v, w)}{|H(u, v, w)|^2\Phi_f(u, v, w) + \alpha\Phi_\eta(u, v, w)} \tag{15}$$

or

$$W(u, v, w) = \frac{\bar{H}(u, v, w)}{|H(u, v, w)|^2 + \alpha(1/\beta)} \tag{16}$$

where $\beta = \Phi_f(u, v, w)/\Phi_\eta(u, v, w)$ is called the signal-to-noise ratio ($SNR$) for the additive and signal-independent noise, $H(u, v, w)$ are the FT of $h(x, y, z)$, the bar denotes complex conjugation, $\alpha$ is the Wiener parameter and $\Phi_f(u, v, w)$ and $\Phi_\eta(u, v, w)$ are the power-spectral densities of the original image and the noise, respectively. Then, for each triple of frequencies, we define a convex set in the form of Eqn (13) as

$$\begin{aligned} C_1(u, v, w) = \{y(x, y, z) :& |W(u, v, w)G(u, v, w) \\ & - Y(u, v, w)|^2 \leq \xi_1(u, v, w)\} \end{aligned} \tag{17}$$

where the expected variation is given by

$$\Psi_1(u, v, w) = \frac{N^3\Phi_\eta(u, v, w)\Phi_f(u, v, w)}{|H(u, v, w)|^2\Phi_f(u, v, w) + \Phi_\eta(u, v, w)} \tag{18}$$

and the bounded variation is

$$\xi_1(u, v, w) = c\frac{N^3\Phi_\eta(u, v, w)\Phi_f(u, v, w)}{|H(u, v, w)|^2\Phi_f(u, v, w) + \Phi_\eta(u, v, w)} \tag{19}$$

The projection of an arbitrary image $i(x, y, z)$ onto $C_1(u, v, w)$ is given by [20]

$$\begin{aligned} i^*(x, y, z) &= \mathbf{P}_{C_1(u,v,w)} \cdot i(x, y, z) \Leftrightarrow I^*(u, v, w) \\ &= \begin{cases} W(u, v, w) \cdot G(u, v, w) - \sqrt{\xi_1(u, v, w)}\frac{\Delta(u,v,w)}{|\Delta(u,v,w)|} & \\ \qquad\qquad \text{if} |\Delta(u, v, w)|^2 \geq \xi_1(u, v, w) & \\ I(u, v, w), \qquad \text{otherwise} & \end{cases} \end{aligned} \tag{20}$$

where $\Delta(u, v, w) = W(u, v, w)G(u, v, w) - I(u, v, w)$ and $I(u, v, w)$ is the FT of $i(x, y, z)$ and $\mathbf{P}_{C_1(u,v,w)}$ is the projector over $C_1(u, v, w)$.

The first set is then defined as

$$\begin{aligned} C_1 = \{y(x, y, z) :& |W(u, v, w)G(u, v, w) - Y(u, v, w)|^2 \\ & \leq \xi_1(u, v, w) \quad \text{for all } u, v, w\} \end{aligned} \tag{21}$$

and the projector over $C_1$ is defined as

$$\mathbf{P}_1 = \mathbf{P}_{C_1(u_1,v_1,w_1)} \circ \mathbf{P}_{C_1(u_2,v_2,w_2)} \circ \ldots \circ \mathbf{P}_{C_1(u_L,v_L,w_L)} \tag{22}$$

Another approach is to modify the set $C_1$ using the filter defined by Goodman and Belsher [29]. They developed a pointwise linear, space-invariant, minimum mean square restoration filter for the Poisson image noise model using the orthogonality principle in the Fourier domain. In [29], the filter was applied to 1D data and in [32] it was applied to 2D images. Here, we apply this approach to 3D volumetric data images. This filter does not take into account the additive and signal-independent noise and it is defined in the Fourier domain as

$$W_{GB}(u, v, w) = \frac{\bar{\mu}\bar{H}(u, v, w)\Phi_f(u, v, w)}{1 + \bar{\mu}|H(u, v, w)|^2\Phi_f(u, v, w)} \tag{23}$$

or

$$W_{GB}(u, v, w) = \frac{\bar{H}(u, v, w)}{|H(u, v, w)|^2 + 1/\gamma} \tag{24}$$

where $\gamma = \bar{\mu}\Phi_f(u, v, w)$ and $\bar{\mu}$ is the ensemble mean number of photon counts. Observe that Eqns (16) and (24) have the same form but, since the Poisson noise is signal dependent, the SNR is not well defined in this case [32]. The prototype image is now obtained by applying this filter over the observed image. Again, for a particular triple of frequencies $(u, v, w)$, the set $C_2(u, v, w)$ is defined as

$$\begin{aligned} C_2(u, v, w) = \{y(x, y, z) :& |W_{GB}(u, v, w)G(u, v, w) \\ & - Y(u, v, w)|^2 \leq \xi_2(u, v, w)\} \end{aligned} \tag{25}$$

and the projection of an arbitrary function $i(x, y, z)$ onto $C_2(u, v, w)$ is

$$i^*(x,y,z) = \mathbf{P}_{C_2(u,v,w)} \cdot i(x,y,z) \Leftrightarrow I^*(u,v,w) = \begin{cases} W_{GB}(u,v,w)G(u,v,w) - \sqrt{\xi_2(u,v,w)}\,\frac{\Delta(u,v,w)}{|\Delta(u,v,w)|} & \text{if } |\Delta(u,v,w)|^2 \geq \xi_2(u,v,w) \\ I(u,v,w) & \text{otherwise} \end{cases} \quad (26)$$

where now $\Delta(u, v, w) = W_{GB}(u, v, w)G(u, v, w) - I(u, v, w)$, and $\mathbf{P}_{C_2(u,v,w)}$ is the projector over $C_2(u, v, w)$. As before, $\xi_2(u, v, w)$ is obtained using the expected variation by $\xi_2(u, v, w) = c\Psi_2(u, v, w)$ where

$$\Psi_2(u,v,w) = \frac{N^3\Phi_f(u,v,w)}{\left|1 + \bar{\mu}|H(u,v,w)|^2\Phi_f(u,v,w)\right|^2} \quad (27)$$

The second set is then defined as

$$C_2 = \{y(x,y,z) : |W_{GB}(u,v,w)G(u,v,w) - Y(u,v,w)|^2 \leq \xi_2(u,v,w) \text{ for all } u,v,w\} \quad (28)$$

and the projector onto $C_2$ is defined by

$$\mathbf{P}_2 = \mathbf{P}_{C_2(u_1,v_1,w_1)} \circ \mathbf{P}_{C_2(u_2,v_2,w_2)} \circ \ldots \circ \mathbf{P}_{C_2(u_L,v_L,w_L)} \quad (29)$$

*Prototype constraint based on a pointwise adaptative smoothness constraint*

The third set implements a pointwise adaptative smoothness constraint, which is also a prototype image constraint and is defined for each triple of spatial coordinates by

$$C_3(x,y,z) = \{y(x,y,z) : \|q(x,y,z) - y(x,y,z)\|^2 \leq \xi_3(x,y,z)\} \quad (30)$$

where, in vector–matrix notation, the prototype $\mathbf{q}$ is defined as $\mathbf{q} = \mathbf{M} \cdot \mathbf{g}$, where $\mathbf{M}$ is a local spatial averaging operator and $\xi_3(x, y, z) = c\Psi_3(x, y, z)$.

It is difficult to determine $\Psi_3(x, y, z)$ because it requires the knowledge of the local autocorrelation sequence of the actual image, but assuming that the noise is stationary, zero-mean white process, it is possible to derive an estimate of $\Psi_3(x, y, z)$ as

$$\hat{\Psi}_3(x,y,z) = \|z\|^2\left(\frac{\delta_g^2(x,y,z) - \delta_\eta^2}{\|h\|^2}\right) + \|m\|^2\delta_\eta^2 \quad (31)$$

where $\delta_g^2(x, y, z)$ is the local variance of the observed image and $\delta_\eta^2$ is the variance of the additive and independent noise. The terms $\|z\|^2$, $\|h\|^2$ and $\|m\|^2$ are defined by

$$\|z\|^2 = \sum_{(i,j)\in S_z} |z(i,j)|^2, \quad \|h\|^2 = \sum_{(i,j)\in S_h} |h(i,j)|^2 \quad \text{and} \quad \|m\|^2 = \sum_{(i,j)\in S_m} |m(i,j)|^2 \quad (32)$$

and $z$, $h$ and $m$ are the kernels of the convolutional operators $\mathbf{Z} = \mathbf{MH} - \mathbf{I}$, $\mathbf{H}$ and $\mathbf{M}$, respectively, where $\mathbf{I}$ is the identity operator and $S_z$, $S_h$ and $S_m$ are the support of the kernels.

The projection of an $i(x, y, z)$ onto $C_3(x, y, z)$ is:

$$i^*(x,y,z)\mathbf{P}_{C_3(x,y,z)} \cdot i(x,y,z) = \begin{cases} q(x,y,z) + \sqrt{\xi_3(x,y,z)} & \text{if } i(x,y,z) > q(x,y,z) + \sqrt{\xi_3(x,y,z)}, \\ q(x,y,z) - \sqrt{\xi_3(x,y,z)} & \text{if } i(x,y,z) < q(x,y,z) - \sqrt{\xi_3(x,y,z)}, \\ i(x,y,z) & \text{otherwise} \end{cases} \quad (33)$$

The third set is then defined as

$$C_3 = \{y(x,y,z) : \|q(x,y,z) - y(x,y,z)\|^2 \leq \xi_3(x,y,z) \text{ for all } x,y,z\} \quad (34)$$

and the projector onto $C_3$ is defined by

$$\mathbf{P}_3 = \mathbf{P}_{C_3(u_1,v_1,w_1)} \mathrm{o} \mathbf{P}_{C_3(u_2,v_2,w_2)} \mathrm{o} \ldots \mathrm{o} \mathbf{P}_{C_3(u_L,v_L,w_L)} \quad (35)$$

*Constraints based on positive and finite extent images*

The fourth set is obtained by imposing the solution to be non-negative since image intensity is always non-negative. This constraint is necessary because the Wiener solution (or the Goodman and Belsher solution) is not necessarily non-negative. Then, the set $C_4$ is defined as

$$C_4 = \{y(x,y,z) : y(x,y,z) \geq 0 \text{ for all } x,y,z\} \quad (36)$$

The projection of an arbitrary $i\,(x, y, z)$ onto $C_4$ is

$$i^*(x,y,z) = \mathbf{P}_4 \cdot i \Leftrightarrow i^*(x,y,z) = \begin{cases} \Re[i(x,y,z)] & \text{if } \Re[i(x,y,z)] \geq 0 \\ 0 & \text{otherwise} \end{cases} \quad (37)$$

where $\mathbf{P}_4$ is the projector over $C_4$.

The last set tries to recover the frequencies that fall into the missing cone frequencies generated by the TF of the imaging system. The idea is that the image has a compact support and all values outside this support are zero values. The set $C_5$ is the set of all functions of finite extent in the three directions and is defined by

$$C_5 = \{y(x,y,z) : y(x,y,z) = 0 \quad \text{for all}\,(x,y,z) \notin S_y\} \tag{38}$$

where $S_y$ is the support of $y(x,y,z)$.

The projection of an arbitrary $i\ (x,y,z)$ onto $C_5$ is

$$\begin{aligned} i^*(x,y,z) &= \mathbf{P}_5 \cdot i(x,y,z) \\ &= \begin{cases} i(x,y,z) & \text{if}\,(x,y,z) \in S_y \\ 0 & \text{if}\,(x,y,z) \notin S_y \end{cases} \end{aligned} \tag{39}$$

where $\mathbf{P}_5$ is the projector over $C_5$.

The approach adopted by this algorithm is similar to the Gerchberg–Papoulis algorithm [33], where one searches for a solution alternating between both space and Fourier domain. We omit here the proof of the convexity and closeness of all the sets, but the reader can find it in [27, 28] for sets like (11) and [20] for sets (36) and (38).

An interesting point observed by Sezan and Trussell is that the assumption of local stationarity made by the pointwise smooth constraint implies that some parts of the image are smoother than others, which suggests that the image is not well represented by a globally stationary random process. This is in contradiction with the global stationarity assumption made by the bounded variation assumed by the Wiener solution constraint. However, stationarity is assumed in the Wiener filter because it is mathematically tractable rather than because it reflects knowledge about an actual random process.

## The Poisson Noise Filtering Procedures

It is well known that the Poisson noise is dominant in images obtained by means of computational optical sectioning. As stated before, in order to use the set $C_1$, we need to reduce or eliminate the level of Poisson noise in the measured data because the Wiener filter does not take it into account. In fact, we will try to reduce the noise and consider the remainder as an independent and additive white noise which is not necessarily a Gaussian process. We suggest two ways to accomplish that. The first one is to find an estimate of the blurred image without the Poisson noise using a MAP filter and the second one is to obtain an approximate solution for this using the Anscombe transformation (AT) [34].

*The map estimation*

Lo [32] derived a MAP filter for the Poisson noise that can be expressed in vector–matrix notation by

$$(\mathbf{q} - \mathbf{1}) - \mathbf{R}_\mathbf{b}^{-1}(\mathbf{b} - \bar{\mathbf{b}}) = \mathbf{0} \tag{40}$$

where $\mathbf{b}$ is the image without the Poisson noise, the elements of $\mathbf{q}$ are $q_i = g_i/b_i$, $\mathbf{g}$ is the version of $\mathbf{b}$ corrupted by noise, $\mathbf{1}$ is a unitary vector, $\mathbf{R}_\mathbf{b}$ is the covariance matrix of $\mathbf{b}$, and $\bar{\mathbf{b}}$ is the non-stationary mean of $\mathbf{b}$. In this paper, we assume that $\mathbf{R}_\mathbf{b} = \sigma_\mathbf{b}^2 \cdot \mathbf{I}$, where $\sigma_\mathbf{b}^2$ is the variance of $\mathbf{b}$ and $\mathbf{I}$ is the identity matrix. Under this assumption, we have a pointwise MAP estimator for the blurred image without the Poisson noise that is given by

$$\hat{b}_i = \frac{(\bar{b}_i - \sigma_b^2) \pm \sqrt{(\bar{b}_i - \sigma_b^2)^2 + 4\sigma_b^2 g_i}}{2} \tag{41}$$

where the positive root is taken because the image intensity is always non-negative.

*The AT approach*

Another approach that we suggest to filter the noise is to use the AT [34]. The AT transforms the signal-dependent Poisson noise into an approximately Gaussian, additive, signal-independent noise with zero mean and unit variance.

The AT on $g_i$ is given by

$$z_i = 2\sqrt{g_i + \tfrac{3}{8}} \tag{42}$$

where $z_i$ can be represented by an additive model as

$$z_i = 2\sqrt{b_i + \tfrac{1}{8}} + v_i = s_i + v_i \tag{43}$$

Now $v_i$ is an additive noise that is approximately independent of $s_i$, Gaussian distributed with zero mean and unity variance. Using these facts, it is possible now to use well-known techniques for reducing signal-independent, additive noise, by operating on the random variables $z_i$ [35]. For instance, we know that under the criterion of minimum mean square error, the linear filter that is optimum is the Wiener filter. After noise smoothing, we return to the original variable applying the inverse AT on $z_i$ which is given by

$$\hat{b}_i = \tfrac{1}{4}z_i^2 - \tfrac{1}{8} \tag{44}$$

Both, the MAP filter in Eqn (41) and the AT approach in Eqn (44), are pointwise procedures, i.e. they do not take into account the correlation among the pixels of the original image. In practice, we observed for the image data sets studied in this work that the AT approach displayed a slightly better performance. However, on the other hand, the filter based on the AT approach cannot be applied to data with less than about 20 photons per pixel [36]. Then, for low counts, we need to use the MAP criterion.

## The POCS Algorithm

We now can define two POCS algorithms that incorporate the above-defined sets. Given a starting image $f^{(0)}$, we search for a solution by the expression

$$f^{(n+1)} = \mathbf{P}_5 \cdot \mathbf{P}_4 \cdot \mathbf{P}_3 \cdot \mathbf{P}_1 \cdot f^{(n)} \tag{45}$$

or

$$f^{(n+1)} = \mathbf{P}_5 \cdot \mathbf{P}_4 \cdot \mathbf{P}_3 \cdot \mathbf{P}_2 \cdot f^{(n)} \tag{46}$$

where $f^{(n+1)}$ is an estimate of the true image and $f^{(0)}$ can be, for example, the observed image (blurred and noisy) or a uniform image. Pre-processing is necessary when using Eqn (45) in order to reduce the Poisson noise and Eqn (46) does not take into account additive, signal-independent noise, because it is not defined into Eqn (23). Figure 2 shows a block diagram of the proposed method.

The relaxed versions of Eqns. (45) and (46) are given by

$$f^{(n+1)} = \mathbf{T}_5 \cdot \mathbf{T}_4 \cdot \mathbf{T}_3 \cdot \mathbf{T}_1 \cdot f^{(n)} \tag{47}$$

or

$$f^{(n+1)} = \mathbf{T}_5 \cdot \mathbf{T}_4 \cdot \mathbf{T}_3 \cdot \mathbf{T}_2 \cdot f^{(n)} \tag{48}$$

where $\mathbf{T}_k = \mathbf{I} - \lambda_{n,k} \cdot (\mathbf{P}_k - \mathbf{I})$ for $\lambda_{n,k} \in (0, 2)$.

## Numerical Results

In this section, we present some simulated and experimental results using a phantom image and also real cell images. The proposed method was implemented in C++ language and runs either on SGI Octane computer with a 250 MHz R10000 processor and 256 MB RAM or on 400 MHz Intel Pentium-II processor with 310 MB RAM. In this work, we present the results using the second hardware configuration. The 3D DFT was implemented using the fast Fourier transform (FFT) algorithm [37] and using the periodogram technique for the power spectrum density estimation of the true image.

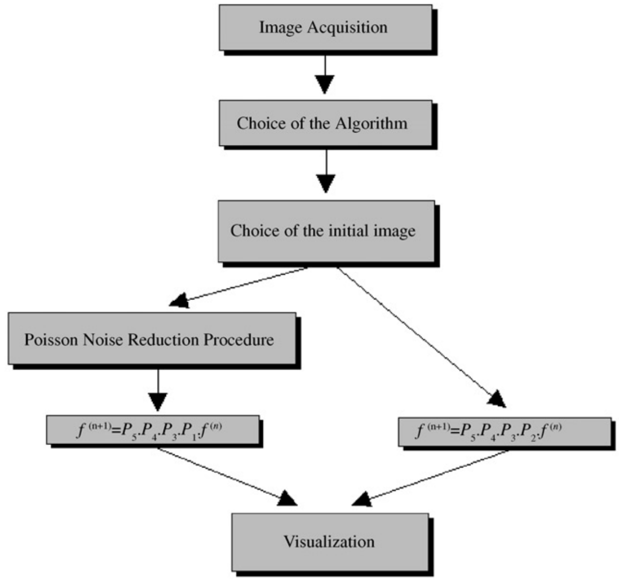


**Figure 2.** Block diagram of the proposed method.

When Eqn (45) is used for real cell processing, the additive noise was considered white and it was estimated under a uniform $3 \times 3 \times 3$ or $5 \times 5 \times 5$ volumetric window over the observed image and, in the case of the phantom processing, we have control over the additive and signal-independent noise. In all cases, we first process the images using one of the proposed procedures to reduce the Poisson noise.

Now, when Eqn (46) is used, the additive, signal-independent noise is not taken into account in the processing, because that procedure does not consider this kind of noise. Also, in this case, no pre-processing is performed in order to reduce the Poisson noise.

All the presented results are obtained without relaxation and considering as initialization the Wiener solution. We assume $c = 1$ for the confidence interval in sets $C_1$, $C_2$ and $C_3$ for all results, which implies 50% of

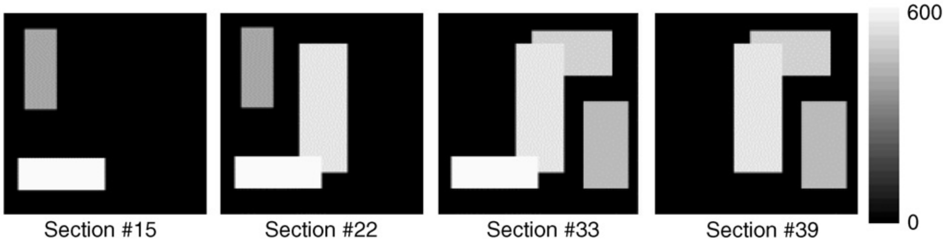


**Figure 3.** $64 \times 64 \times 64$ phantom image.

confidence in the case of distributions that are symmetric about their mean.

A 3D phantom was used to evaluate the performance of the algorithm consisting of a $64 \times 64 \times 64$ image with several square structures, which was chosen because of its variations along all three dimensions and sharp edges. The pixel size in the $x$ and $y$ directions is 0.094 microns (μm) and in the $z$ direction is 0.25 μm. In order to simulate a standard non-confocal microscope, a theoretical PSF was calculated with the Gibson and Lanni model [38] using the Washington University XCOSM software [33]. This PSF corresponds to a 60X oil-immersion objective lens with a numerical aperture of 1.4 and we consider that the phantom has a fluorescence wavelength of 535 nm.

In order to quantify the restoration results, a performance measure was computed based on the improvement in signal-to-noise ratio (*ISNR*) in decibels (dB) which is defined by the equation

$$ISNR = 10 \log \frac{\sum_{j=1}^{N^3} (f_j - g_j)^2}{\sum_{j=1}^{N^3} (f_j - \hat{f}_j)^2} \qquad (49)$$

where $f_j$ is the $j$th element of the phantom image $\mathbf{f}$, in vector–matrix notation, $\hat{f}_j$ is the $j$th element of the restored image $\hat{\mathbf{f}}$ and $g_j$ is the $j$th element of the degraded phantom image $\mathbf{g}$.

Figure 3 shows four slices of the phantom through the $z$ direction and Figures 4 and 7 show the corresponding blurred slices by the PSF and degraded by signal-dependent Poisson noise. Also, the images are degraded by additive, signal-independent Gaussian noise at 5 dB in Figure 4 and at 10 dB in Figure 7. Figures 5 and 6 present the results using the image in Figure 4 as the observed image and Figures 8 and 9 present the results using the image in Figure 7 as the observed image. The idea is to show the preformance of the algorithm for two different levels of noise.

Figure 5 presents the results using Eqn (45) after the pre-processing using the MAP filter and the AT approach where the number of iterations were 19 and 20 until the convergence, respectively. For the processing using the MAP filter, the ISNR was 13.93 dB and the execution time was 4.5 min and for the processing using the AT approach the ISNR was 14.64 dB and the execution time was 4.5 min. Figure 6 presents the results using Eqn (46), where the number of iterations was 19 until the convergence and the ISNR was 13.40 dB. The execution time in this case was 4 min.

Figure 8 shows the results using Eqn (45) after the pre-processing using both the filtering noise procedures, where the number of iterations were 18 and 20 until convergence, respectively. Now, for the processing using the MAP filter, the ISNR was 13.90 dB and the execution time was 4.5 min and for the processing using

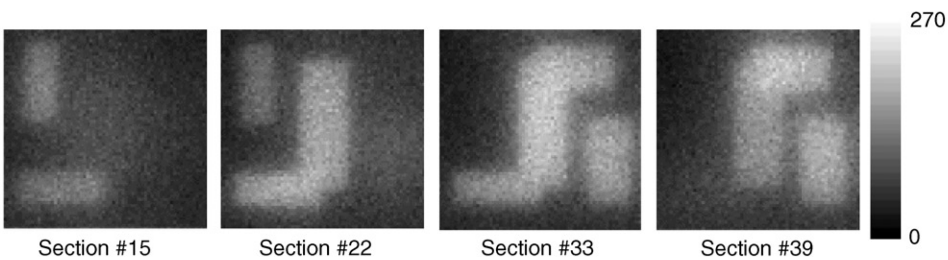


**Figure 4:** Sections through the simulated microscopic data degraded by the signal-dependent Poisson noise and also by the additive, signal-independent Gaussian noise at 5 dB.

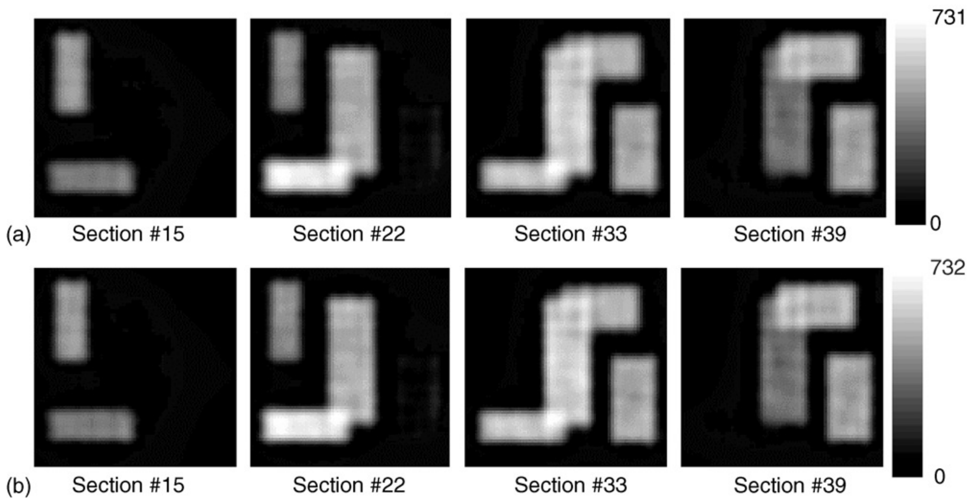


**Figure 5.** (a) Sections of the restored image using Eqn (45) pre-processed by the MAP filter. The ISNR was 13.93 dB. (b) Sections of the restored image using Eqn (45) pre-processed by the AT filter. The ISNR was 14.64 dB.

the AT approach, the ISNR was 14.57 dB and the execution time was 4.5 min. Figure 9 presents the results using Eqn (46), where the number of iterations was 20 until the convergence, the ISNR was 13.25 dB and the execution time was 4 min. Although the AT approach demonstrated a better performance in the reduction of the Poisson noise, we note that the final results after the processing with the POCS algorithm, using both the filtering noise procedures, were similar for the two different levels of additive, signal-independent noise presented in this work.

Figure 10 shows an example for a 3D real neuron image (retinal ganglion cell) acquired using a fluorescence two-photon microscope. Figure 10(a) shows two sections of the blurred and noisy neuron and Figure 10b shows the result of the processing using Eqn (46). Figure 11(a) shows two sections of a tobacco cell 3D image acquired using a fluorescence standard non-confocal microscope and Figure 11(b) shows the respective processed sections using Eqn (45), where the AT approach was used in the pre-processing. The images in Figures 10 and 11 were bleach corrected before processing.

## Discussions

In the simulation tests, both the POCS methods presented here have a fast convergence rate in the sense that they only need few iterations to produce acceptable results and allowed visual results substantially close to the phantom. Also the overall ISNR for the restored images indicates a good performance of the methods. The results show that the algorithms are robust with respect to high level of noise and they are able to recover most of the edges of the square structures into the phantom and improve the contrast of the image. As one can see, in the real case, the algorithm is also capable of removing most of the blurring by improving the contrast

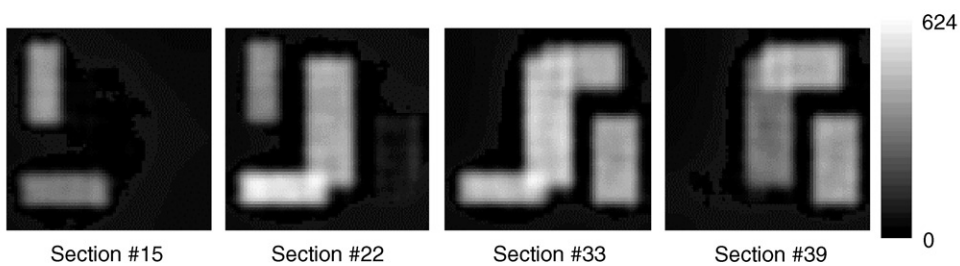


**Figure 6.** Sections of the restored image using Eqn (46). The ISNR was 13.40 dB.

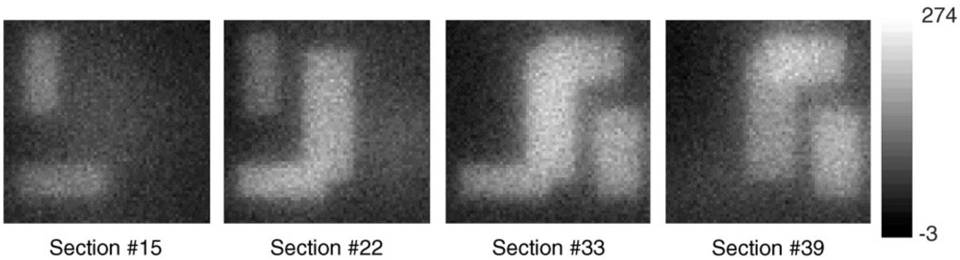


**Figure 7.** Sections through the simulated microscopic data degraded by the signal-dependent Poisson noise and also by the additive, signal-independent Gaussian noise at 10 dB.

and also reducing the noise in the image. Another interesting observed fact is that, for most of the considered processed images, the visual results after only a few iterations (for instance, five iterations) were similar to the final result, which suggests that the processing can be interrupted before the convergence in order to accelerate the processing time. Observe that we present results without relaxation, so that the convergence rate could also be achieved by varying the relaxation parameter.

As stated before, we have used the periodogram technique for the power spectrum density estimation. However, it is well known that the periodogram is a biased estimate of the power spectrum and we expect that the quality of results could be further improved by using more accurate techniques of estimation. It is important to observe that our implementation of the proposed method is not optimized and therefore we also expect that the execution times described here can also be improved using more efficient routines for the projections and also using faster codes for the fast Fourier transform algorithms.

Another interesting point to note is that the size of the prototype constraint sets increases with the $c$ values, and if one uses higher levels of confidence (for instance, $c = 2$ or 3), the algorithm may converge faster, but it may not significantly improve the initial image because the constraints become less restrictive [27]. On the other hand, choosing smaller values for $c$ may result in non-intersecting sets and the serial cyclic algorithm POCS does not converge to the solution. We have found that $c = 1$ is a good choice for the images in this work.

One can observe that distinct results can be obtained for different initial images. In fact, we could choose an arbitrary image to initialize the POCS algorithm. For

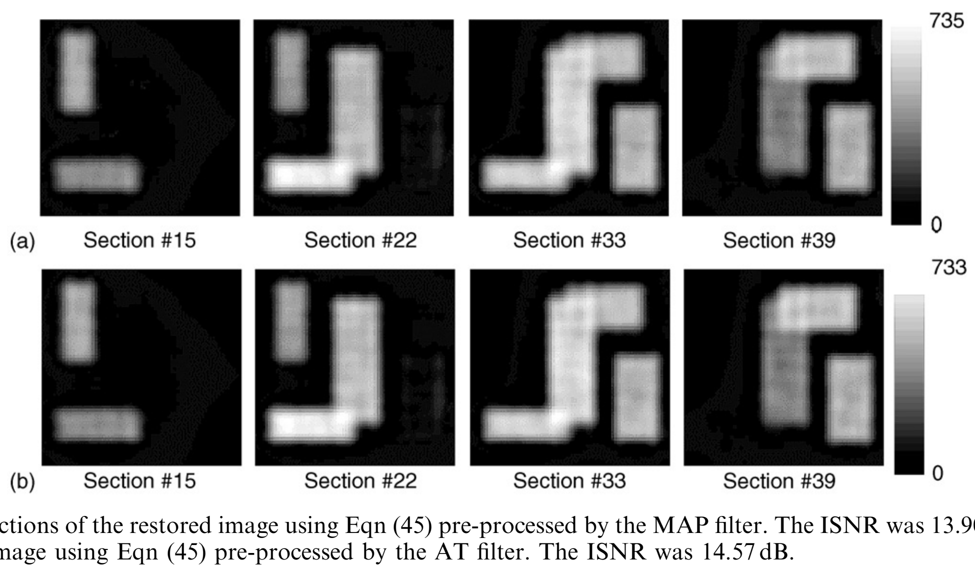


**Figure 8.** (a) Sections of the restored image using Eqn (45) pre-processed by the MAP filter. The ISNR was 13.90 dB; (b) Sections of the restored image using Eqn (45) pre-processed by the AT filter. The ISNR was 14.57 dB.

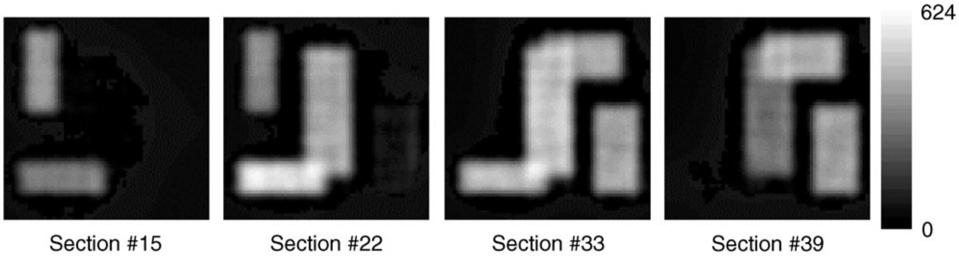


**Figure 9.** Sections of the restored image using Eqn (46). The ISNR was 13.25 dB.

instance, we could use a uniform image, the blurred and noisy image, the blurred image without noise or even the Wiener solution. In this work, we have obtained good results with the Wiener solution as an initial estimate. However, we have tested the algorithm for other initial images and no significant changes were observed in the final results.

Better results can be achieved by varying the parameter of the Wiener filter. As stated before, we used a biased estimate of the power spectrum density of the image and by varying the parameter of the Wiener filter it is possible to improve the $SNR$ of the filtered image. For instance, the Wiener parameter in Eqn (15) was set at 0.1 for the images in Figures 5 and 8. For this reason, we also multiply the term $1/\gamma$ into Eqn (24) by a constant parameter. For instance, for the results in Figures 6 and 9 we have multiplied $1/\gamma$ by 0.5.

The advantage of Eqn (45) is that it takes into account the additive, signal-independent noise and the disadvantage is that it needs pre-processing in order to reduce the Poisson noise which implies more computational cost. However, we have observed that Eqn (45) is robust for

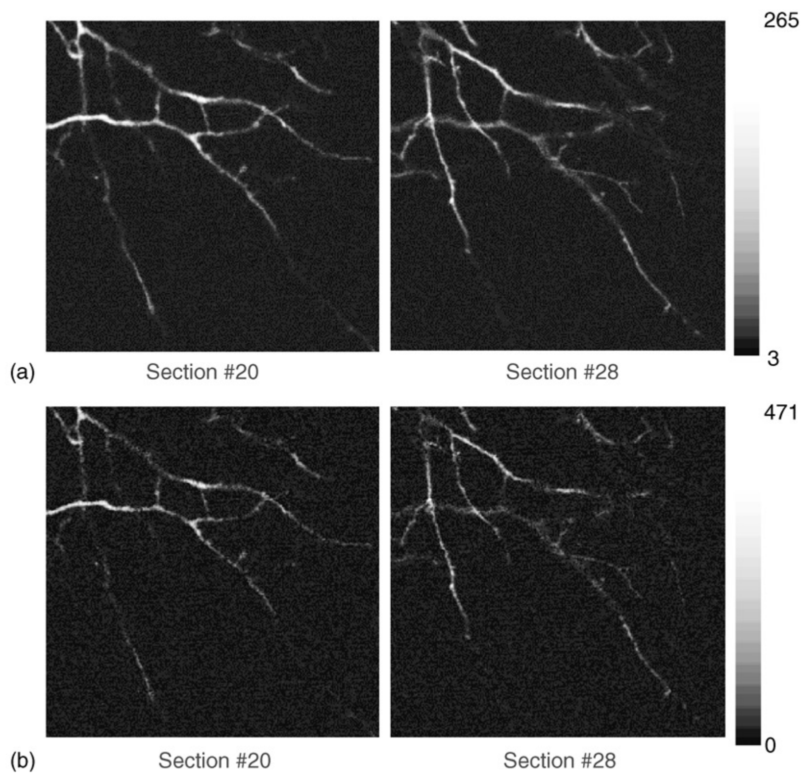


**Figure 10.** (a) Sections of a $256 \times 256 \times 64$ pixels neuron image (retinal ganglion cell) acquired by using a two-photon fluorescence microscope; (b) Sections of the restored neuron image using Eqn (46).

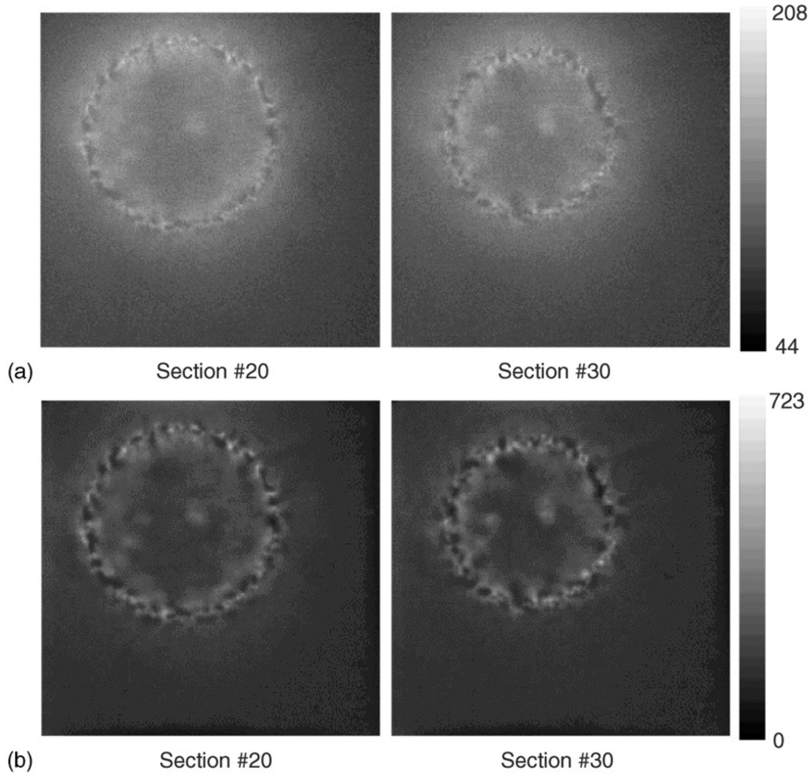


**Figure 11.** Sections of a $256 \times 256 \times 64$ pixels image of the tobacco cell acquired by using a conventional widefield fluorescence microscope: (a) blurred and noisy image; and (b) restored image using Eqn (45) pre-processed by the AT approach.

low level of Poisson noise which suggests that in this particular case we can use the method without the pre-processing step, consequently decreasing the processing time.

On the other hand, as one can see from the results, Eqn (46) is also robust in the presence of additive, signal-independent noise. It is well known that in COSM, the prevalent noise is Poisson and the other sources of noise do not significantly degenerate the image and, perhaps for this reason, the algorithm is able to produce good results in the presence of this kind of noise. One can expect that, in general, if it is known that the image is strongly degraded by additive, signal-independent noise, an additional effort to remove that could be necessary in order to achieve good results with Eqn (46). We are still investigating this aspect of the proposed algorithm. However, when the observed image is strongly corrupted by the Poisson noise, as an alternative in the use of Eqn (46), we also suggest the use of pre-processing in order to reduce the noise although this procedure increases the overall processing time.

## Concluding Remarks

We have presented a fast iterative algorithm based on the projections theory, where we have demonstrated the capability of the projection onto convex sets approach applied to the computational optical-sectioning problem. Although we used the serial cyclic POCS, the cost–benefit of the method is particularly good because of the fast convergence rate (even without relaxation) and visual results obtained with a simulated phantom and with real cell images. In this sense, the method can be a good choice for the deconvolution of microscopic images. Nowadays, there are more effective techniques to implement the POCS algorithm in order to improve the convergence rate, as for instance, parallel projections methods using approximate projections and extrapolated iterations beyond the interval (0,2) [18]. In order to further improve the results, we intend to extend the method presented in this work using more accurate projections methods and with faster convergence rate than the serial cyclic POCS, including parallel implementation for cell deconvolution.

## Acknowledgments

The authors would like to thank Prof. Donald L. Snyder from ESSRL of the Electrical Engineering Department and Prof. Barbara Pickard from the Biology Department, both from Washington University in St Louis, USA, for offering the facilities of their laboratories and also for their helpful discussions. We also thank Prof. Rachel Wong of the Anatomy and Neurobiology Department from Washington University for the neuron images, as well. This work was supported by a Brazilian scholarship from FAPESP (grant number 99/01351-2), and by a FINEP-RECOPE grant number 77.97.0575.00.

## References

1. Costa, L.F. (1995) Computer vision based morphometric characterization of neural cells. *Review of Scientific Instruments* **66**: 3770–3773.
2. Agard, D.A. (1984) Optical sectioning microscopy: cellular architecture in three dimensions. *Annual Reviews of Biophysics and Bioengineering* **13**: 191–219.
3. Swedlow, J.R.; Sedat, J.W. & Agard, D.A. (1997) Deconvolution in optical microscopy. In: Jansson, P.A. (ed.), *Deconvolution of Images and Spectra* (2nd edn) New York: Academic Press, pp. 284–309.
4. Conchello, J.A. & Hansen, E.W. (1990) Enhanced 3-D reconstruction from confocal scanning microscope images. 1: Deterministic and maximum likelihood reconstructions. *Applied Optics*, 29(26): 3795–3804.
5. McNally, J.G., Conchello, J.A., Rosenberger, F.U., Preza, C. & Markhan, J. (1996) Tutorial-Image Restoration for 3-D Microscopy. April 26–27, IBC, Washington University, St. Louis, MO.
6. Weinstein, M. & Castleman, K.R. (1971) Reconstructing 3-D specimens from 2-D section images. In: Herron, R.E. (ed.), *Quantitative Imagery in the Biomedical Sciences I. Proceedings of the SPIE* **26**: 131–138.
7. McNally, J.G., Karpova, T., Cooper J. & Conchello J.A. (1999) Three-dimensional imaging by deconvolution microscopy. *Methods* **19**: 373–385.
8. Verveer P.J., Gemkow M.J. & Jovin, T.M. (1999) A comparison of image restoration approaches applied to three-dimensional confocal and wide-field fluorescence microscopy. *J. Microsc.* **193:** 50–61.
9. Preza, C., Miller, M.I. & Conchello, J.A. (1992) Image reconstruction for 3-D light microscopy with a regularized linear method incorporating a smoothness prior. Acharya, R.S. & Goldgof, D.B. (eds), *IS&T/SPIE Proceedings.* 129–139.
10. Preza, C., Miller, M.I., Thomas, L.J. & McNally, J.G. In: Regularized linear method for reconstruction of three-dimensional microscopic objects from optical sections. *Journal of the Optical Society America A* **9**: 219–228.
11. McNally, J.G., Preza, C., Conchello, J.A., Thomas, Jr., L.J. (1994) Artifacts in computational optical-sectioning microscopy. *Journal of the Optical Society America A* 11(3): 1056–1067.
12. Markham J. & Conchello, J.A. (2001) Fast maximum-likelihood image-restoration algorithms for three-dimensional fluorescence microscopy. *Journal of the Optical Society America A* 18(5): 1052–1071.
13. Dempster, A.P., Laird, N.M. & Rubin D.B. (1977) Maximum likelihood from incomplete data via the EM algorithm. *J. R. Statist. Soc. B* **39**: 1–38.
14. Joshi, S. & Miller, M.I. (1993) Maximum *a posteriori* estimation with Good's roughness for optical sectioning microscopy. *Journal of the Optical Society America A* **10**: 1708–1085.
15. Conchello, J.A. & McNally, J.G. (1996) Fast regularization technique for expectation maximization algorithm for computational optical sectioning microscopy. In: Cogswell, C.J. Kino, G.S. & Wilson, T. (eds), *Three-Dimensional Microscopy: Image Acquisition and Processing*, *SPIE* **2655**: 199–208.
16. Conchello, J.A. (1998) Super-resolution and convergence properties of the expectation-maximization algorithm for maximum-likelihood deconvolution of incoherent images. *Journal of the Optical Society of America A* **15**: 2609–2620.
17. Combettes, P.L. (1993) The foundations of set theoretic estimation. *Proceedings of the IEEE* **81**: 182–208.
18. Combettes, P.L. (1996) The convex feasibility problem in image recovery. In: Hawkes, P. (ed.), *Advances in Imaging and Electron Physics*, Vol. 95. New York: Academic Press, pp. 155–270.
19. Combettes, P.L. (1992) Convex set theoretic image recovery: history, current status, and new directions. *Journal of Visual Communications an Image Representation* **3**: 307–315.
20. Stark, H. & Yang, Y. (1998) *Vector Space Projections, a Numerical Approach to Signal and Image Processing, Neural Nets, and Optics*. New York: Wiley.
21. Stark, H. & Sezan, I.M. (1994) Image processing using projetion methods. In: Javidi, B. & Horner, J. (eds), Real Time Optical Information Processing Orlando, FL: Academic Press, Inc, pp. 185–232.
22. Sezan, M.I. (1992) An overview of convex projections theory and its application to image recovery problems. *Ultramicroscopy* **40**: 55–67.
23. Youla, D.C. & Webb, H. (1982) Image restoration by the method of convex projections: Part 1 – theory. *IEEE Transaction Medical Imaging* **MI-1**: 81–94.
24. Koshy, M., Agard, D.A. & Sedat, J.W. (1990) Solution of toeplitz systems for the restoration of 3-D optical sectioning microscopy data. In: Smith, L.C. (ed.), *Bioimaging and Two-Dimensional Spectroscopy*, *Proceedings of the SPIE* **1205**: 64–71.
25. Lenz, R. (1986) 3-D Reconstruction with a projection onto convex sets Algorithm. *Optics Communications* **57**: 21–25.
26. Gopalakrishman, V.K., Ramachandran, R.P., Wilder, J. & Mammone, R.J. (1999) Restoration of three dimensional images using the row action projection method. *IEEE International Symposium on Circuits and Systems*, Orlando, FL, pp. 33–36.
27. Sezan, M.I. & Trussell, H.J. (1991) Prototype image constraints for set-theoretic image restoration. *IEEE Transactions on Signal Processing* **39**: 2275–2285.
28. Sezan, M.I. & Tekalp, A.M. (1990) Adaptative image restoration with artifact suppression using the theory of

convex projections. *IEEE Transactions on Acoustics Speech, Signal Processing* **38**: 181–185.
29. Goodman, J.W. & Belsher, J.F. (1976) Fundamental limitations in linear invariant restoration of atmospherically degraded images. *Proceedings of SPIE* **75**: 141–154.
30. Gibson, S.F. & Lanni, F. (1989) Diffraction by a circular aperture as a model for three-dimensional optical microscopy. *Journal of the Optical Society of America A* **6**: 1357–1367.
31. Snyder. D.L., Hammoud, A.M., & White, R. (1993) Image recovery from data acquired with a charge-couple-device camera. *Journal of the Optical Society of America A* **10**: 1014–1023.
32. Lo, C.M. (1979) Estimation of image signals with Poisson noise. *Doctoral Thesis*, University of Southern California.
33. Papoulis, A. (1975) A new algorithm in spectral analysis and bandlimited extrapolation. *IEEE Transactions on Circuits and Systems* **CAS-22**: 735–742.
34. Anscombe, F.J. (1948) The transformation of Poisson, binomial and negative-binomial data. *Biometrika* **15**: 246–254.
35. Mascarenhas, N.D.A., Santos, C.A.N. & Cruvinel, P.E. (1999) Transmission tomography under Poisson noise using the Anscombe transformation and Wiener filtering of the projections. *Nuclear Instruments and Methods in Physics Research A* **423**: 265–271.
36. Starck, J.L. & Murtagh, F. (2001) Astronomical image and signal processing. *IEEE Signal Processing Magazine*, March, 30–40.
37. Press, W.H., Teukolshy, S.A., Vetterling, W.T. & Flannery, B.P. (1992) *Numerical Recipes in C* (2nd edn). Cambridge: Cambridge Univ. Press.
38. Gibson, S.F. & Lanni, F. (1991) Experimental test of an analytical model of aberration in an oil-immersion objective lens used in three-dimensional light microscopy, *Journal of Optical Society of America A* **8**: 1601–1613.
39. XCOSM (version 2.4)-available from http://3dmicroscopy.wustl.edu/xcosm.